

The M 4 Core Project with *HST* – V. Characterizing the PSFs of WFC3/UVIS by Focus^{*}

J. Anderson¹ and L. R. Bedin²

¹Space Telescope Science Institute, 3700 San Martin Dr., Baltimore, MD 21218, USA

²Istituto Nazionale di Astrofisica - Osservatorio Astronomico di Padova, Vicolo dell'Osservatorio 5, Padova, IT-35122

Accepted 2017 May 19. Received 2017 May 19; in original form 2017 April 19

ABSTRACT

As part of the astrometric *Hubble Space Telescope* (*HST*) large program GO-12911, we conduct an in-depth study to characterize the point spread function (PSF) of the *Uv-VISual channel* (*UVIS*) of the *Wide Field Camera 3* (*WFC3*), as a necessary step to achieve the astrometric goals of the program. We extracted a PSF from each of the 589 deep exposures taken through the F467M filter over the course of a year and find that the vast majority of the PSFs lie along a one-dimensional locus that stretches continuously from one side of focus, through optimal focus, to the other side of focus. We constructed a focus-diverse set of PSFs and find that with only five medium-bright stars in an exposure it is possible to pin down the focus level of that exposure. We show that the focus-optimized PSF does a considerably better job fitting stars than the average “library” PSF, especially when the PSF is out of focus. The fluxes and positions are significantly improved over the “library” PSF treatment. These results are beneficial for a much broader range of scientific applications than simply the program at hand, but the immediate use of these PSFs will enable us to search for astrometric wobble in the bright stars in the core of the globular cluster M 4, which would indicate a dark, high-mass companion, such as a white dwarf, neutron star, or black hole.

Key words: globular clusters: individual (M 4, NGC 6121)

1 INTRODUCTION

One of the Hubble Space Telescope’s (*HST*’s) great advantages is that it has an extremely stable point-spread function (PSF) relative to ground-based telescopes. The fact that *HST* is in orbit high above the atmosphere means that the PSF that is delivered to the detector is free of turbulence-related variations: the PSF varies more spatially across the detector than it does temporally. The spatial variations are due to a combination of geometric optics and detector-related features (such as variable charge diffusion due to changes in chip thickness, see Krist 2003).

For the case of the *Uv-VISual channel* (*UVIS*) of the *Wide Field Camera 3* (*WFC3*) —on which the present investigation is focused—a set of 7×8 fiducial PSFs arrayed across the detector is necessary to map these variations. In

other words, the PSF can change significantly over about 500 detector pixels. (Sabbi & Bellini 2013).

Even though the *HST* PSF is not beset by atmospheric variations, the fraction of light in the *HST* PSF core can vary with time by $\pm 3\%$ due to “breathing”, the focus variations that result as *HST* changes orientation relative to the Sun or goes into and out of the Earth’s shadow during its orbit. This has been explored in numerous documents (see Dressel 2014 for a summary).

A proper understanding of the *HST* PSF is critical for many high-precision *HST* studies. With an accurate PSF, systematically accurate positions can be measured for well-exposed stars to better than 0.01 pixel (~ 0.4 mas) enabling a large number of astrometric applications. Also, an accurate PSF is critical for weak-lensing analyses and deconvolution-type analysis of barely-resolved or blended sources.

One of the reasons that the *HST* PSF has not been characterized very well thus far stems from the fact that it is undersampled. When a detector is not at least Nyquist-sampled, that means its pixels are too wide to capture all the spatial information in the scene that the telescope is delivering to the detector (see Lauer 1999). Each exposure

* Based on observations with the NASA/ESA Hubble Space Telescope, obtained at the Space Telescope Science Institute, which is operated by AURA, Inc., under NASA contract NAS 5-26555, under Large Program GO-12911.

gives us a limited amount of information about the scene, and we must combine multiple dithered exposures in order to fully represent all the information delivered by the telescope to the detector. This is equally true for the scene and for the PSF: we need to combine multiple dithered images to fully understand either of them.

Unfortunately, it is particularly complicated to combine multiple dithered exposures with *HST* on account of its large optical distortion. Even dithers of 10 pixels cannot be combined without careful attention to the forward and reverse distortion solutions, since a shift of 10.0 pixels at the center of the detector can correspond to 10.2 pixels at the edge.

Anderson & King (2000, AK00) developed a detailed procedure whereby a set of dithered exposures can be used to extract a properly sampled PSF model from a series of undersampled images. AK00 further demonstrate that this PSF can be used to extract accurate and unbiased positions for stars in a single exposure. This initial procedure was constructed for *Wide Field Camera 2 (WFPC2)*, but it has since been generalized to two out of three channels of the *Advanced Camera for Surveys (ACS)*'s, namely the *High Resolution Channel (HRC)* and the *Wide Field Channel (WFC)*, see Anderson & King 2004, Anderson & King 2006) and to both the WFC3 channels (UVIS and the *Near Infra-Red, NIR*, Anderson 2016).¹

The AK00 procedure shows how to construct a PSF for a particular data set, and the PSF should in principle be valid only for the particular *average* state of the telescope during those exposures. Fortunately, in practice, it turns out that breathing affects the *HST* PSF in specific ways that often do not affect our ability to do astrometry or photometry (if we allow for a possible shift in zeropoint of ± 0.03 magnitude and *general* linear astrometric transformations). For this reason, Anderson has constructed a set of “library” PSFs for various filters and detectors from data-sets that are well suited for PSF reconstruction (a large number of high S/N unsaturated stars and several dithered exposures). These PSFs can be used to extract differential positions good to better than 0.01 pixel and differential photometry good to better than 0.01 magnitude (see Bedin et al. 2013).

As such, many projects do not require tailor-made PSFs, but can be done with a static archive of library PSFs. Other projects, however, do require more than just simple differential astrometry or photometry on well-separated stars. Such more complicated projects rely on the PSF either to do simultaneous fitting to multiple overlapping stars (such as in crowded fields or resolved-binary studies) or to do a deconvolution-type fitting of resolved objects (such as in weak-lensing studies of field galaxies). For these purposes, better PSF models are necessary.

Unfortunately, many of the projects for which static library PSFs are not adequate do not have enough bright, well-exposed stars in the field to allow construction of a full spatially variable model of the PSF. (It typically requires over 560 high-signal-to-noise stars in an image, i.e., enough

to get 10 stars in each of the 7×8 spatially independent PSF zone.)

If the *HST* PSF varies in an irregular way from exposure to exposure, then there will be no way to do these star-poor yet PSF-dependent projects. However, if it can be shown that the *HST* PSFs fall largely into a one-parameter family regulated by the telescope focus and breathing, then it may be possible to construct a set of library PSFs, parametrized by focus. In that case, rather than needing enough stars in an image to extract a full spatially variable PSF, it may be possible to specify only one parameter: the telescope focus. This would allow high-precision PSF-based analyses for a great many exposures that heretofore have been amenable only to less rigorous analyses.

In this article, we will determine whether such a family exists for F467M (the main filter of our *HST* large program GO-12911, see Sect. 3) and, if so, how easy it will be to pinpoint the focus, and thus specify the full PSF, for a given exposure. If this procedure works for our data set in one filter, then perhaps it could be performed for other filters in other data sets as well.

2 THE PILOT STUDY FOR WFC3/UVIS/F606W

An initial study of how the PSF responds in detail to changes of focus is documented in Anderson et al. (2015, A15). This study made use of the fact that the upper-left corner of the detector is known to be out of focus relative to the rest of the detector, thus making that corner more sensitive than the rest of the detector to variations of focus.

When the telescope goes from one side of focus to the other, the PSF changes are symmetric to first order: some flux is transferred from the diffraction rings to the core and then back again. To break this degeneracy, we need to explore higher-order PSF changes. Models show that when the telescope is on one side of focus, the PSF is slightly astigmatic in one sense, then on the other side of focus its astigmatism is the opposite.

It is worth noting that the undersampled nature of the *HST* PSF makes it particularly difficult to explore this asymmetry, since all the changes happen within the star's inner 3×3 pixels, and the exact location of a star's center within its central pixels has a much larger impact on the distribution of these 3×3 pixel values than does the PSF variation with focus. As such, it is critical to model the average PSF well enough to examine these small perturbations and explore how the higher-order aspects of the PSF change with focus.

The investigation in A15 went through the entire WFC3/UVIS archive and identified all the exposures that had a good number of stars in the focus-sensitive upper-left corner. They isolated those stars that were centered nearly perfectly on their central pixels so that it would be easy to construct metrics to measure the residual astigmatism using a simple moment-based analysis. Next, they fit each of these stars with a pre-existing “library” PSF for the F606W filter so that they could construct residuals which could be distilled into a relative sharpness and a relative astigmatism. When the authors of A15 plotted the astigmatism against the sharpness of the PSF, they found that the PSF var-

¹ All geometric distortions, library PSFs, and the codes that use these to extract positions and fluxes are publicly available at <http://www.stsci.edu/~jayander/>

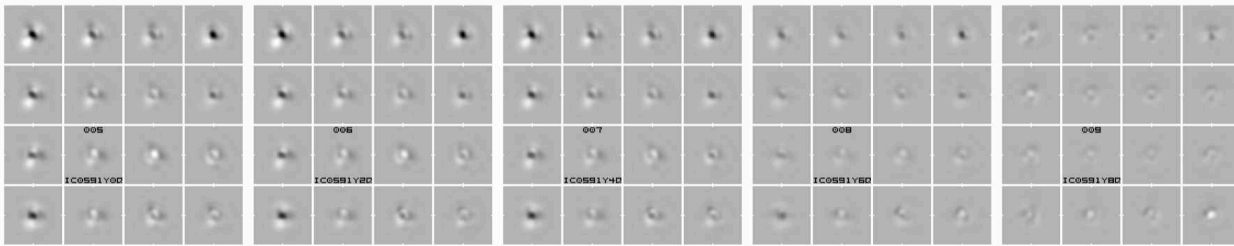


Figure 1. The 4×4 perturbation PSFs for five consecutive exposures in the epoch-11 data set. The exposure name and number in the 49-image series for the epoch are given for each. Dark corresponds to more flux than the library PSF, white to less flux. The perturbation PSF changes systematically during the sequence of exposures.

ied along a simple “banana”-like path in this two-parameter space (see Figure 7 of A15).

The fact that there is such a tight empirical relationship between astigmatism and sharpness means that the PSFs apparently come from a simple one-parameter family. It was further found that all of the star images from a given exposure clustered in a single location along this curve and stars from different exposures clustered in different locations. This led us to conclude that the different locations along the curve correspond to different focus levels of the telescope.

The next step was to group together exposures that had the same focus and extract images of unsaturated but well-exposed stars (i.e., those with between 5×10^4 and 3×10^5 total counts) that were in the upper-left corner. A15 then used these extracted images of actual stars to construct an average PSF for the upper-left corner, one for each of eight different focus levels, thus arriving at an empirical picture of how the PSF changes. Figure 13 of A15 shows this variation visually. It is clear that the PSF goes from being asymmetric in the $+135^\circ$ direction at their first focus level, to being asymmetric in the $+45^\circ$ direction at the other side of focus, at their focus-level 8.

This limited study of the F606W PSF in the upper-left-corner of the WFC3/UVIS detector was an encouraging indication that it should be possible to characterize the PSF across the entire detector in terms of focus. This is clearly the next step to take.

3 THE NEXT STEP

Because of the undersampled nature of the PSF, we need to have multiple observations of point sources at multiple sub-pixel locations if we hope to construct an accurate super-sampled model of the PSF. The fact that the PSF changes spatially across the detector means that we need many stars in each spatially-coherent zone. Anderson & King (2000) showed that, in addition to this, we also need a way to determine an accurate position for each PSF-contributing star. All of this means that we require multiple dithered images, each of which has a large number of stars. Globular clusters have served as the ideal targets for this purpose.

As such, large program GO-12911 (PI: Bedin) is perfect for such a study. Its main focus is to do high-precision astrometry of stars in globular cluster M4 over the course of 12 months with an aim to measure the astrometric wobble of main-sequence stars that may have heavy unseen

binary companions (such as black holes, neutron stars, or white dwarfs). Bedin et al. (2013, Paper I) provides for an overview.

The observations are divided into 12 epochs, spaced roughly a month apart. Each epoch consists of ~ 49 deep observations with WFC3/UVIS through the medium-band F467M filter, wherein the turnoff is just below the level of saturation, thus providing the maximum number of high signal-to-noise stars. The F467M filter was chosen so that the ideal exposure time would be just over 339s, which is the threshold for efficient buffer-dumping with WFC3/UVIS. The program also took short exposures in filter F775W to provide colors, as well as short exposures in F467M to provide some handle on the evolved population. But we focus here on the 589 deep exposures through F467M taken in 120 single-orbit visits between 9 October 2012 and 16 September 2013.

4 GROUPING THE OBSERVATIONS BY FOCUS

4.1 Using all the stars

Even though the upper-left corner is more sensitive to changes in focus than the rest of the detector, in reality the PSF across the entire detector changes when the focus changes, and there is surely more information in the entire detector than in just the upper left sixteenth of the detector. It is hard, though, to use the moment-based analysis that worked in the upper-left corner across the entire chip, since different locations across the detector are at different places along the local focus curve. For this reason, we sought a way to extract an estimate of the full spatially variable PSF for each exposure.

We noted above that we would need at least 560 well-exposed-but-unsaturated stars in an image if we hope to constrain the array of 7×8 PSFs with a minimum of ten stars in each fiducial-PSF region. This is a lot to ask for, even in the central field of a globular cluster, where the center of the cluster is often too dense to hope for isolated stars and the outskirts too sparse to get enough stars. For this reason, we decided to first construct a time-averaged “library” F467M PSF that included the full array of 7×8 fiducial PSFs and use that as the basis for the PSF model in each exposure. Then for each exposure, we constructed a “delta” PSF to describe how the PSF in that exposure is different from the time-averaged basis PSF. Such an approach allows the well-constrained average model to deal

with the fine-scale detector-related variations (traceable to issues such as static distortion, or chip thickness and charge diffusion or vignetting) while at the same time accounting for the low-spatial-frequency variations due to focus.

The “basis” PSF model for WFC3/UVIS is similar to that constructed in 2006 for ACS/WFC in Anderson & King (2006), except that instead of using an array of 9×5 PSFs across each 4096×2048 chip, we adopt a 7×4 array since that better matches the structure present in the UVIS PSF. In particular, this array placement allows a fiducial PSF to be centered on the “happy bunny” location where the PSF is the sharpest (see Sabbi & Bellini 2013, SB13). The PSF at each of the 56 (7×8) fiducial locations is represented by 101×101 super-sampled grid, as in AK00. The super sampling is $\times 4$ with respect to the image pixels, so that the entire PSF goes out to about 12.5 pixels from the center of a star. Even with such dense sub-sampling, it is necessary to use a bi-cubic spline to evaluate the PSF at locations in-between the grid points.

The net empirical PSF that we construct for each exposure consists of the average PSF described above plus a spatially variable 4×4 perturbation tailored to better fit the bright stars in t exposure. The perturbation PSF for each exposure is constructed by identifying a number (typically a hundred or more) of bright and isolated stars across the image. Each of these bright stars is fitted with the “library” PSF appropriate for its location in the image, and the model PSF is subtracted, leaving an array of scaled residuals with respect to the center of each star. These residuals show the difference between the image’s true PSF and the library PSF. We distill these residuals into an 4×4 array of fiducial PSFs (with fiducial PSFs at the corners and edges, so that there is never any extrapolation). Figure 1 shows the perturbation part of the PSF for five exposures in the eleventh epoch.

This 4×4 array of perturbations was combined with the original library PSF to construct a full 7×8 array of PSFs for each exposure. The aim is then to see whether or not this group of PSFs covering the full year of exposures can be generalized into a 1-parameter family.

We naturally start out not knowing the focus level for any of the exposures. Although there is some engineering data that may be able to estimate the PSF focus (Cox & Niemi 2011), it is not clear how accurate the PSF predictions are, and it is not clear how to tie them to accurate spatially variable models. It is possible that the relative-focus measurements we extract from this paper may make it possible to make better use of engineering data.

The task of generalizing these 589 individual-exposure PSF models into a family might lend itself to some kind of principal component analysis, but it is not clear that the variations due to focus would be linear. So, instead of exploring that strategy we sought something simpler and more empirical.

4.2 “Phylogram” plots

We compared the 7×8 array of PSFs from each individual exposure against the corresponding-zone PSFs for every other individual exposure. To do this, we computed the absolute value of the difference between the 7×8 arrays of PSFs

for images i and j as:

$$d_{ij} = \frac{1}{56} \times \sum_{IJ} \left(\sum_{XY} |\psi_{IJXY;i} - \psi_{IJXY;j}| \right) \quad (1),$$

where X and Y go from 1 to 101 covering the Δx and Δy domain of the PSF, and I (J) goes from 1 to 7 (8), corresponding to the spatial variation of the PSF. These simple difference estimates should tell us which exposures have PSFs that are more similar to each other (small d_{ij}) and which have PSFs that are more different from each other (large d_{ij}). Figure 2 shows the distribution of the 589×589 ($\sim 350,000$) d_{ij} values. Most PSFs differ by about 0.05 (equivalent a 5% shift of the flux from one place in the PSF to another), but there is a significant tail that differs by more than 10%, and some that differ by more than 20%.

In the field of biology, it is common to characterize the difference between two species in terms of the total “difference” of the DNA code that represents them. Multiple species can be inter-compared on a “phylogram”, a two-dimensional plot that represents graphically the multi-dimensional differences among the various species in terms of differences between points in a 2-dimensional space. Such diagrams show, for instance, how similar humans are to chimpanzees, dolphins, and paramecia.

In the present study, we also have a large number of data sets that have been characterized by their differences in some quantitative domain. It is worth investigating whether such a two-dimensional graph could be useful in this case as well.

We explored several approaches to constructing such an optimized phylogram-type plot. Of course no two-dimensional plot can do a perfect job representing the myriad of differences among the PSFs, but our aim is to construct the best possible two-dimensional plot that represents these differences. In phylogram-type plots, the distance between species is representative of the log of the number of differences in their DNA sequences. Here, we seek a diagram where the two-dimensional “distance” between two PSFs in our plot is representative of d_{ij} , the difference computed above.

We devised several strategies for coming up with such a diagram and show one such strategy in Figure 3. The goal is to place each point such that its distance (in Δ PSF terms) represents how different the PSFs are. The x and y axes in this space are arbitrary, but the distance between two points is representative of how similar the PSFs are.

We start with the representative of how different the PSFs are. We start with the first exposure at $(x_1, y_1) = (0, 0)$. For the second exposure, we explore all possible trial locations (x_2, y_2) between $(-0.3 : 0.3, -0.3 : 0.3)$, spaced by 0.001 and determine the difference between d_{12} (which happens to be 0.025) and r_{12} (which we define to be $\sqrt{(x_2 - x_1)^2 + (y_2 - y_1)^2}$). We identify the minimum of $E_2 \equiv |d_{12} - r_{12}|$ to be the best location to place the second exposure relative to the first; the quantity E represents the difference between the distance as measured in the plot and the distance measured between the PSFs. The upper left plot in Figure 3 shows the contours of E . There is a circle (shown in green) of best-placement locations for exposure #2, since d_{12} equals r_{12} along the circumference of this circle, and E_2 has its minimum value of 0.0. We adopt an arbitrary point in this circle as the best placement location for exposure #2.

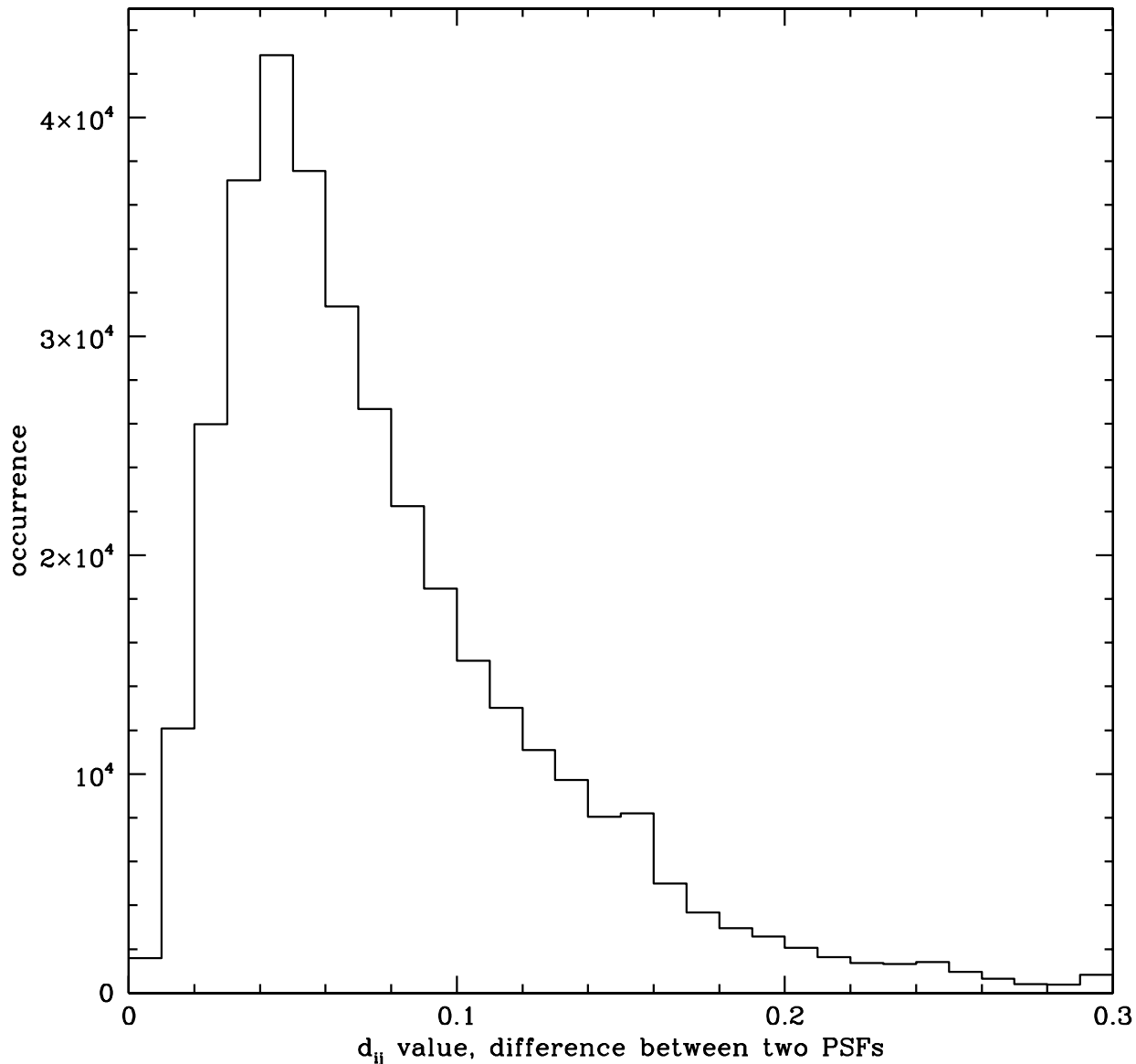


Figure 2. The distribution of values for d_{ij} , which represents the difference between the PSFs extracted from two different exposures. A value of 0.1 means that 10% of the flux from one PSF would have to be re-distributed to arrive at the other PSF.

Once exposure #2 is placed, we can perform the same operation to determine where best to place the third exposure. The middle panel on the left shows the contour plot for E_3 (defined to be $\sum_{n=1}^{3-1} |d_{n3} - r_{n3}|$). The previous points are shown in red and the lowest contour is shown in green. The third exposure (shown in blue) is placed at the location with the lowest value of E_3 . After each new placement, we explore the local neighborhood around each point to see whether it might have a lower value of E by shifting by 0.001 in any direction.

The other panels in Figure 3 show the optimal location to place exposures #4, #24, #105, #106, #315, #340, and #443, based on all the previous placements. It is clear

that the exposures naturally self-organize into a relatively orderly sequence. Figure 4 shows how the placement of each exposure evolves as subsequent exposures are added. We explored several different starting positions for all the stars and several different orders for adding the stars and they all produced a qualitatively similar diagram (modulo a rotation).

In the end adopted Figure 5 as our reference phylogram. We have re-centered and oriented the points for ease of presentation. The 589 points are situated such that their distance from each other best represent the difference in the respective PSFs. The shape of this curve is interesting. It is not simply a straight line, but rather it has a strong curvature to it. This means that the PSFs at the ends are more

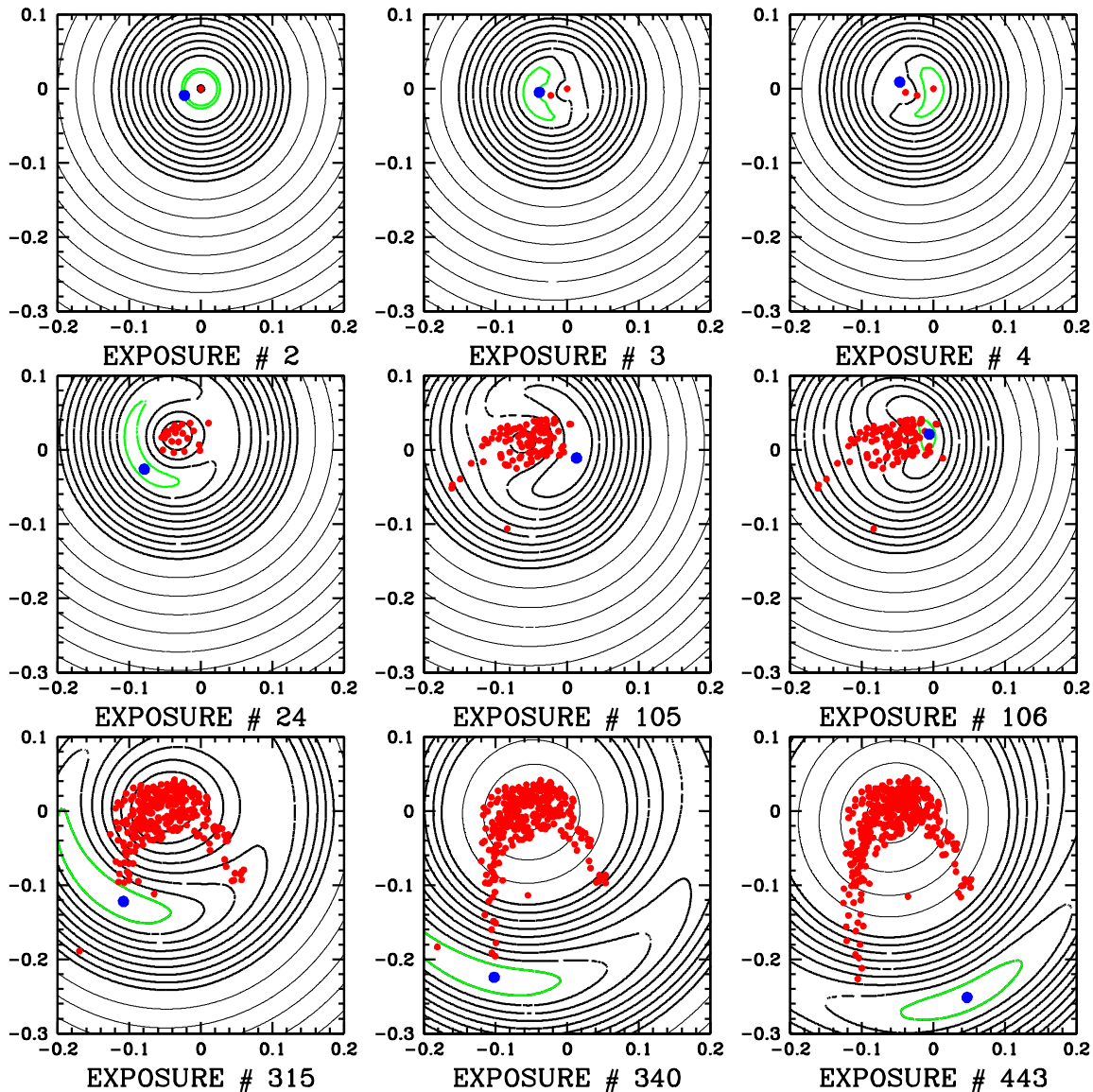


Figure 3. The panels show the construction of the phylogram by adding one exposure at a time. Each panel shows the previously added exposures in red. The contours identify the best location to place the current exposure with respect to the previous exposures such that the computed d_{ij} (the distance between the PSFs) is as close as possible to r_{ij} (distance between the points on the graph). The axes are arbitrary, but their scale represents that of d_{ij} , namely how much flux would have to be moved to go from one PSF to another.

different from the PSFs in the middle than they are from each other. This is in agreement with what we saw in the banana plots from Figure 7 of A15: when the PSF is in focus, it has a maximal fraction of its flux in its central pixel, but this fraction goes down in a similar way on both sides of focus. The PSF is not identical, however, on the different sides of focus, as indicated by distance between the two sides of the wishbone.

Since there are a few outliers from the trend, we investigate several possible causes. We extracted the jitter file for each exposure and determined an RMS with respect to

the average pointing. In Fig. 5 observations with large jitter are shown in red. We also determined which of the observations were able to be placed in a location on the plot that was a good representation of the difference in their PSFs. The two-dimensional plot allowed most observations to be placed such that $E \equiv \sum |d - r|$ is small, but some observations (see left inset) were not. Perhaps this is an indication that a third dimension might exhibit even more order, but since these observations are few, we chose to ignore them and focus on the those that followed the majority trend.

Figure 6 shows the same phylogram-type plot, but in

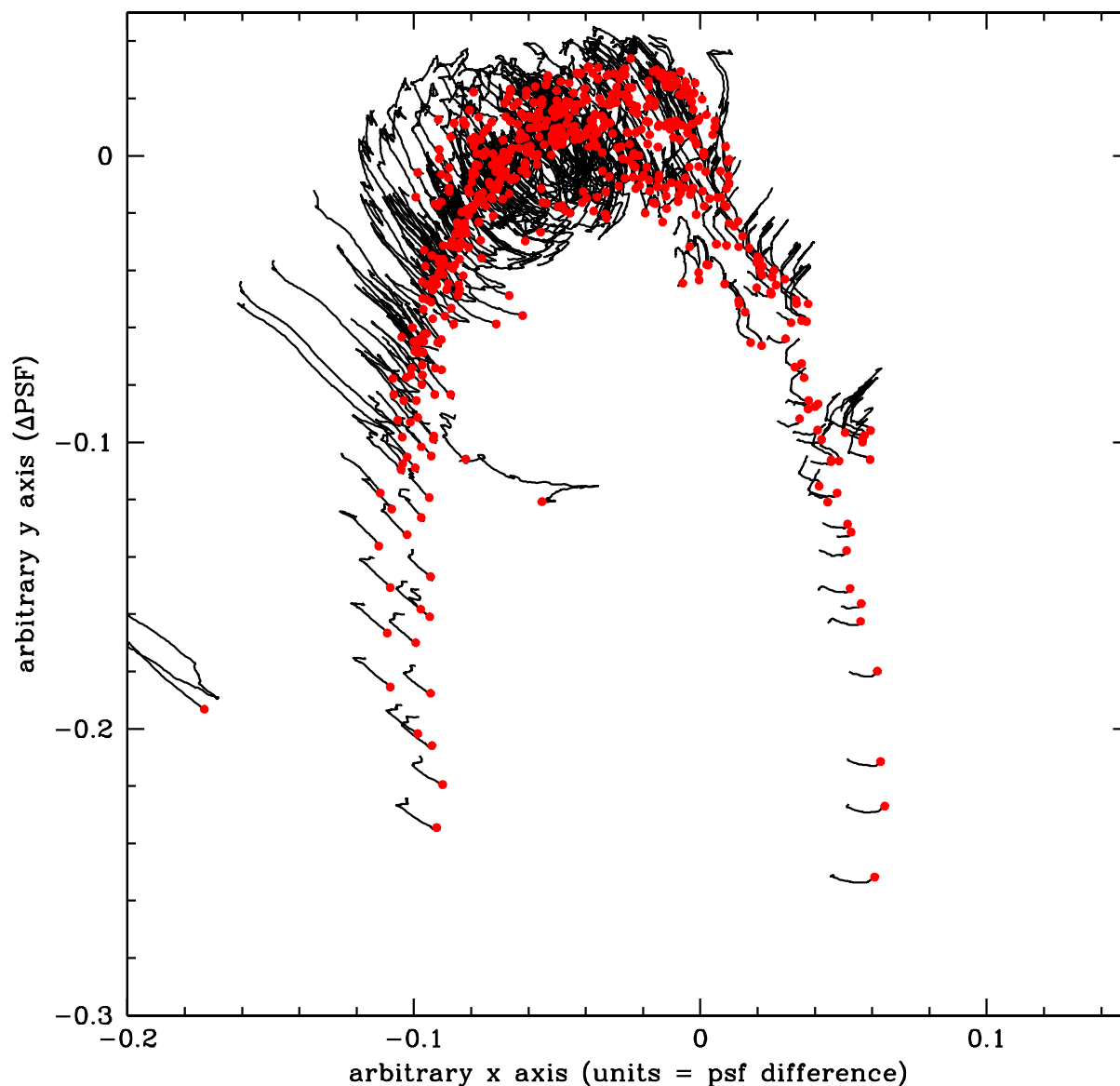


Figure 4. The panels show how the placement of the exposures in the phylogram plot change as more point are added to the diagram. The open end of each black curve show the initial placement of each exposure (based on the preceding exposures), and the red dot at the other end shows the final, optimal resting place for the exposure, after its position has been allowed to creep slowly as more and more points are added.

each of the small panels we highlight in red the observations that correspond to a particular epoch. The epochs are spaced about a month apart and the visits within each epoch span between 21 and 45 hours. It is clear that the PSF is not constant over an epoch, though the PSFs do typically vary over a relatively narrow part of the entire focus range during an epoch. There is no clear progression over time from month to month.

Several visits in Epoch 2 do not follow the focus curve. Inspecting the images, we see that several of them suffered from guide-star failures. Indeed, this is borne out by an in-

spection of the jitter files. All the other epochs follow the well-worn focus path to within 0.02 (corresponding to a 2% average difference between the PSFs, meaning that to get from one PSF to another one would have to rearrange about 2% of the flux).

Now that we are able to characterize individual exposures in terms of where they lie along the focus curve, we can group together exposures at similar focus levels. Figure 7 shows the same points as in Figure 5, but this time we have color-coded those observations at each focus level. We have drawn in a fiducial line for the focus curves and

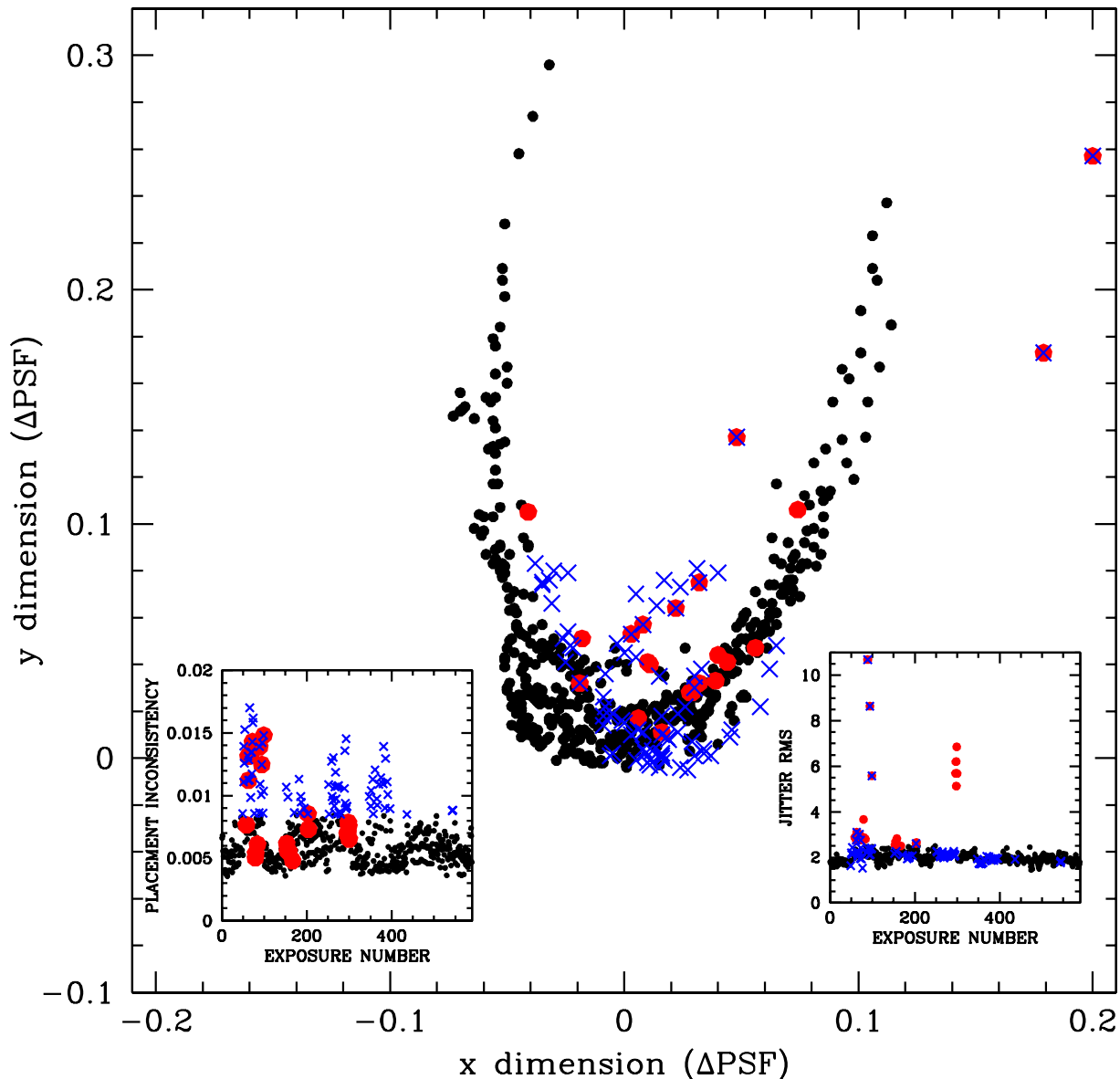


Figure 5. This is the final reference phylogram-type plot where each exposure is represented by a dot, and the dots are separated by “distances” that correspond to the difference between their PSFs. The axes are arbitrary, but units for this are in terms of the average absolute difference between the PSFs (d_{ij} , such that 0.1 means that to get from PSF to another you have to rearrange 10% of the flux. The inset at the lower left shows E_{\min} for each exposure. Stars with low E_{\min} have consistent placement with respect to most of the other exposures. Points are marked blue if they have a high value of E_{\min} . The inset in the lower right shows the jitter RMS for each exposure. Exposures with more pointing jitter than typical are flagged in red.

consider all observations within about 0.02 (98% PSF agreement) of the focus curve to be representative. We arbitrarily divide the curve into 11 distinct focus zones and color-code black the odd zones and in different colors the even ones. The open circles denote the few observations that did not follow the general focus trend as well as the others (mostly during second epoch) that suffered major guiding failures. The first focus group had 4 exposures and the last group 5, but the other groups had between 7 and 150 representative exposures. Focus groups at the extremes naturally have

fewer exposures, reflecting the fact that most of the times the telescope is on focus.

4.3 Finding a PSF for Each Focus Level

The next step was to take all the exposures associated with a given focus group and determine an average PSF for each group. AK00 shows that in order to derive an accurate PSF from stellar profiles, we must have accurate positions and fluxes for each star in each exposure. In undersampled im-

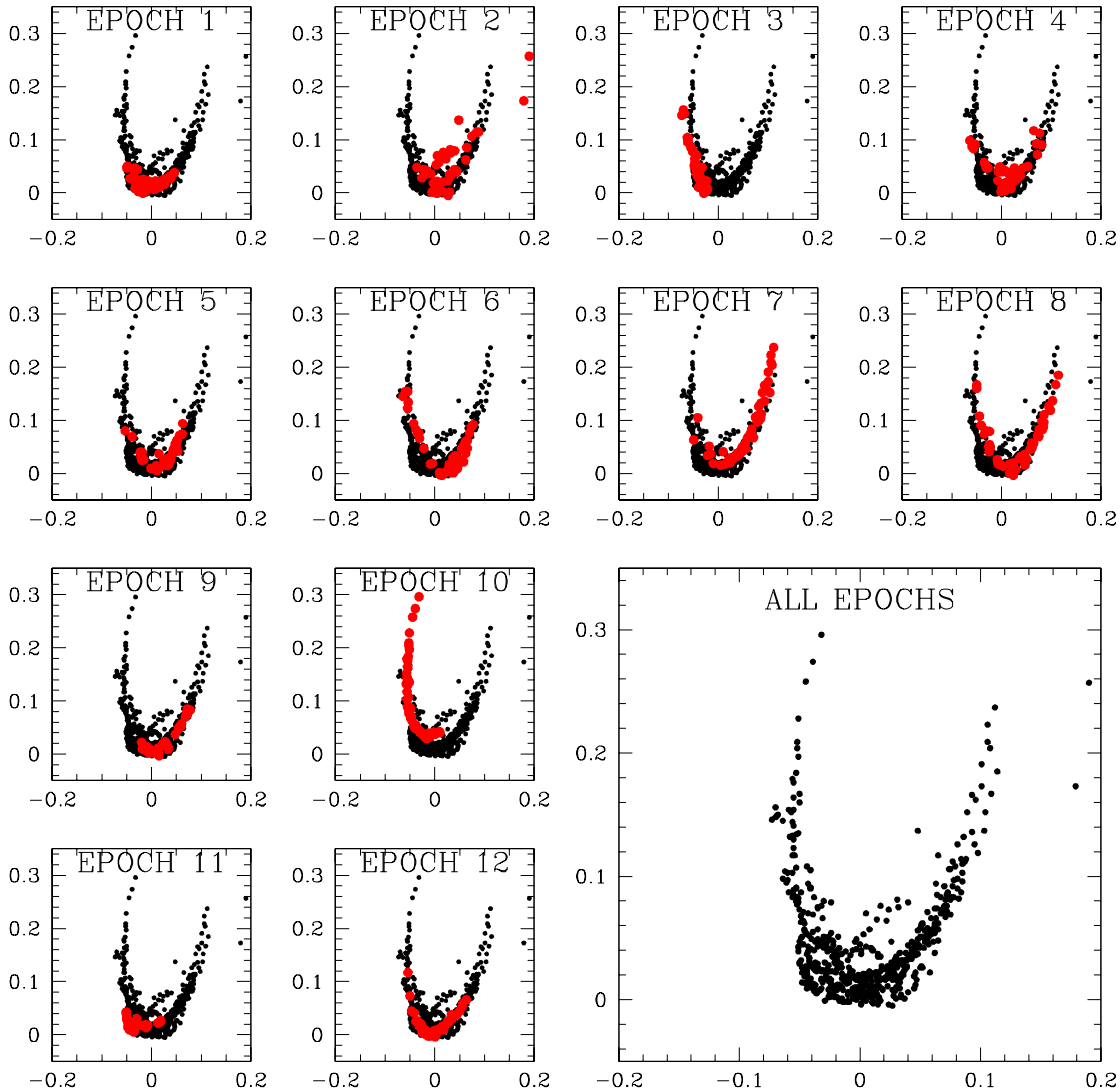


Figure 6. This plot shows in black the same points as in Figure 5, but for each of the 12 epochs it highlights the 49 exposures taken during that epoch.

ages, it is hard to determine accurate unbiased positions, so AK00 developed a procedure to take a dithered set of data and iterate between the solution for PSF and for the positions and fluxes of the stars in a virtuous cycle.

Here, we simply determined a position for each star using the average “library” PSF and determined the flux by means of the total amount of light within a 5-pixel radius. This is considerably larger than the 5×5-pixel fitting region, since we wanted to include flux that landed outside of the fitting region.

With positions and fluxes in the unresampled `_flc` im-

ages², we can extract a spatially variable PSF from the set of exposures associated with each focus zone. As mentioned earlier, there were between 4 and 150 exposures in each zone.

Since we are now extracting detailed PSF models, it is beneficial to illustrate specifically where each fiducial PSF is located on the detector. As we mentioned before, each chip is covered by an array of 7×4 fiducial PSFs, as such the PSFs are spaced by 682 pixels. We place PSFs at the

² The `_flc` images are produced by the STScI archive pipeline. They are `_flt` images corrected from imperfect charge-transfer efficiency (CTE) with an algorithm essentially based on the one presented in Anderson & Bedin (2010).

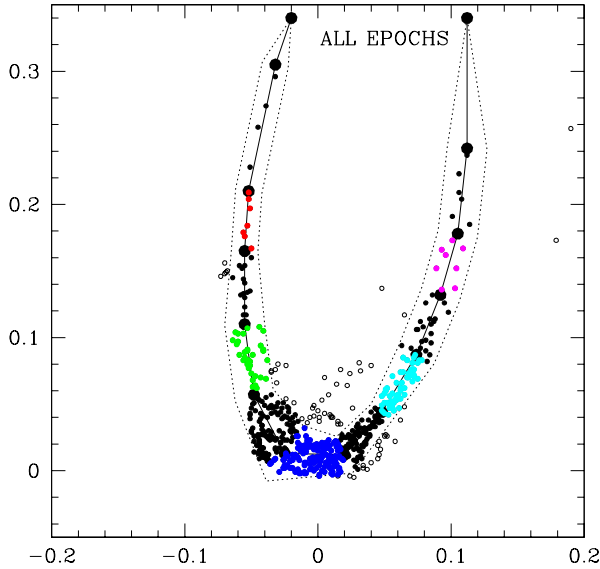


Figure 7. This plot shows the specified zones along the phylogram-type focus curve.

edges and corners of each chip in order to avoid the need for extrapolation. The PSF is linearly interpolated in between fiducial locations but is not assumed to be continuous across the intra-chip gap. Figure 8 shows the locations for the fiducial PSFs for our UVIS PSF model.

The next figure (Figure 9) provides a snapshot of the data that went into our PSF models. From AK00, the PSF model tells us the fraction of a star’s light that should fall in pixel $[i, j]$ relative to its center at (x_*, y_*) . We can thus model the star with the following equation:

$$P_{ij} = z_* \times \psi(i - x_*, j - y_*) + s_*,$$

where z_* and s_* are the star’s total flux and background sky value, respectively. This is the equation for a line, where the slope is the flux and the intercept is the sky. We can invert this to solve for the PSF at a single point in its domain $(\Delta x, \Delta y)$ from the value of pixel $[i, j]$:

$$\psi(\Delta x, \Delta y) = (P_{ij} - s_*)/z_*,$$

where $\Delta x = i - x_*$ and $\Delta y = j - y_*$. Each pixel in each star’s image thus provides an estimate of the PSF at one particular location in its domain.

When we allow for spatial and focus variations, we see that the PSF is now a 5-dimensional function: $\psi(\Delta x, \Delta y; i, j; f)$. To visualize it, we will consider two dimensions at a time. In Figure 9, we plot the samples from the center of the PSF ($|\Delta x| < 0.25$ and $|\Delta y| < 0.25$) for the middle focus level ($f=6$) as a function of detector i coordinate for six horizontal slices across the detector (shown in Fig 8).

We see that even for the “optimal” focus level, the fraction of light in the central pixel can vary from 0.175 to 0.225, more than $\pm 10\%$. There is clear structure on ~ 500 -pixel scales. The peak at the bottom of the detector corresponds to a region with enhanced fringing called the “happy bunny” (SB13).

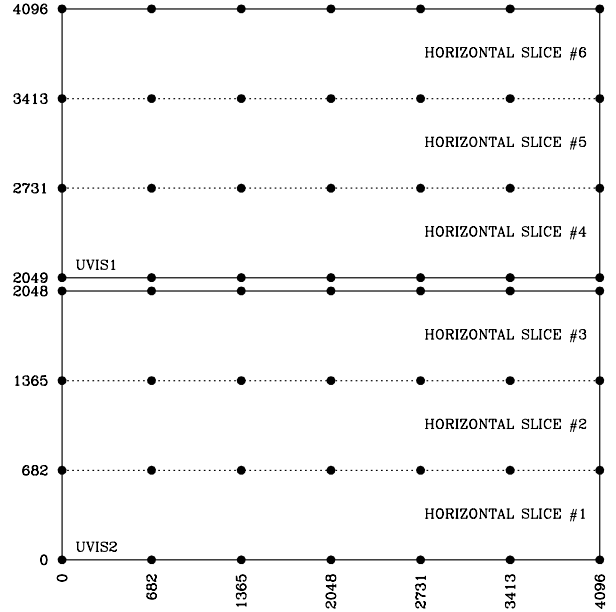


Figure 8. This plot shows the locations of the fiducial PSFs across the two WFC3/UVIS detectors. The useful part of each chip is 4096×2048 pixels and for each of the two an array of 7×4 PSFs is sufficient to map the spatial variation; i.e., for a total of 7×8 PSFs across the entire field of view. Note that there are PSFs at the edges and corners so that no extrapolation will ever be necessary. The PSF is allowed to be discontinuous across the gap between the chips. The horizontal-slice labels pertain to the next plot.

The solid blue dots and connecting lines show the actual PSF model across each strip. The dark-blue line does not represent the data perfectly, but it is good to better than 0.5%.

On the right, we show the same connected points for the central-focus sample ($f=6$ in dark blue, as on the left) and also show the extracted-model points for the two most extreme focus levels, $f=1$ and $f=11$ in green and cyan, respectively. These green and cyan curves are almost everywhere lower than the dark-blue curve, which is consistent with them being much more out of focus. The central value of the PSF in the extreme focus curves varies from 0.13 to 0.18.

The previous figure showed how the central pixel of the PSF varies with position and focus. Figure 10 shows the entire central region of the PSF for the middle focus level ($f=6$). In each of the 7×8 panels we show the inner 5×5 flc-image-pixel region of the PSF (the inner 21×21 PSF grid-points) in terms of their residual with respect to the average PSF across the detector for $f=6$. Black corresponds to more flux than average and white corresponds to less flux. It is clear that there is a large sweet spot in the middle of the detector, and the PSF becomes less tight towards the edges of the field, particularly in the upper-left corner, which we know to be very sensitive to changes in focus. The sharp “happy bunny” feature from SB13 at the bottom is also clear.

The next figure, Figure 11, shows how the PSF varies

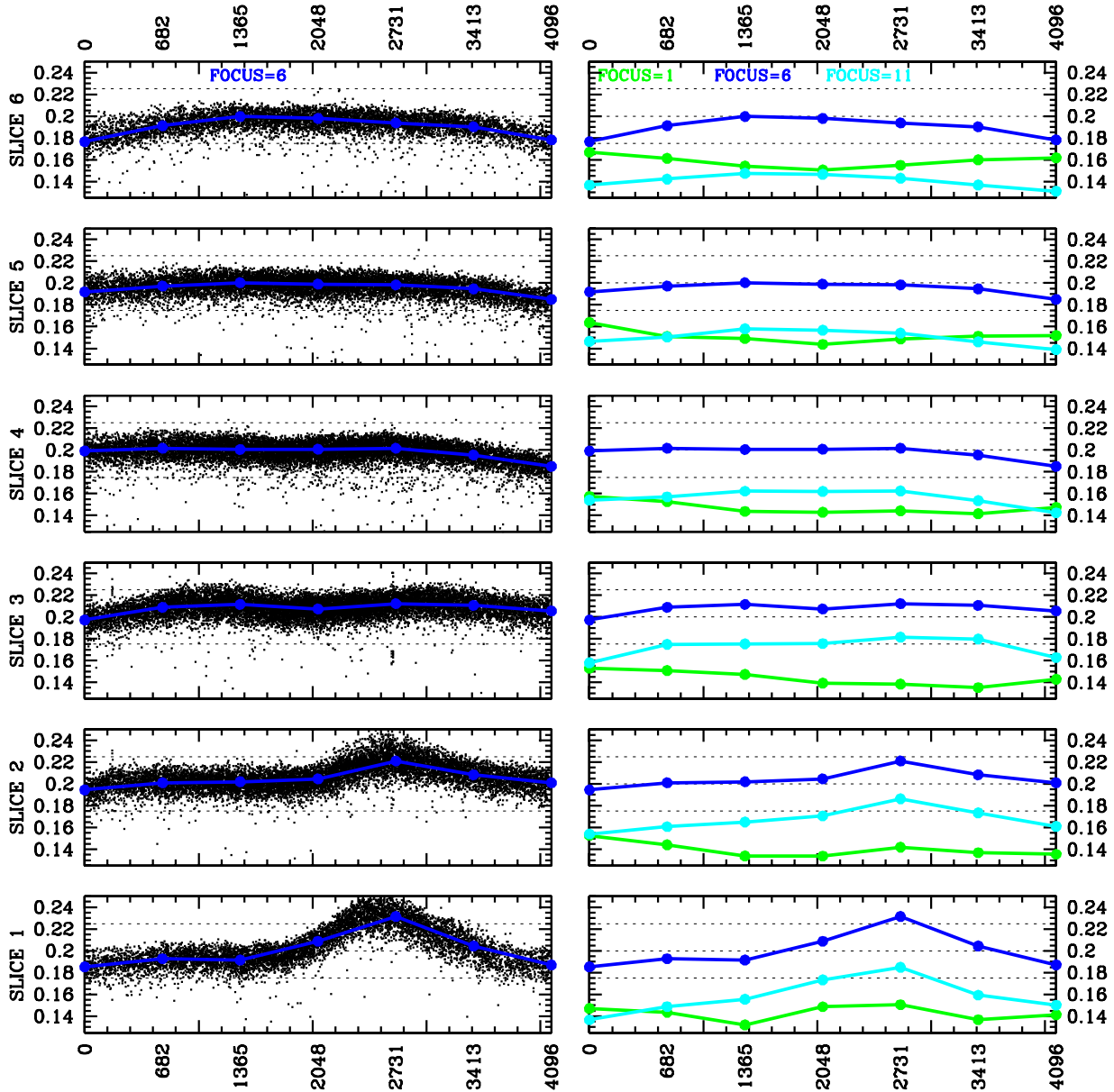


Figure 9. The left plot shows the estimates of the central value of the PSF as a function of x within 6 horizontal slices across the chips (as shown in the previous figure). The individual points correspond to estimates of the central value of the PSF from individual stars in individual exposures that happen to be centered on a pixel to within ± 0.25 pixel in x and y . The units on the left therefore refer to the fraction of a star’s light that would land in its central pixel if the star is centered on that pixel. The individual exposures here are all taken from the group with focus level 6 (the middle of the focus range). The solid blue dots show the value of the function for the fiducial locations of the PSF. The line simply shows the linearly interpolated value between the fiducial locations. The right plot shows these blue (focus=6) points along with the points for the most extreme focus location on one side of focus (green, focus=1) and the other side of focus (cyan, focus=11).

with focus for 7 different locations on the detector. It is clear that in the center of the detectors (the top two panels) the middle focus position has the sharpest PSF, and the PSF gets worse on either side of focus. This is true for the “happy bunny” location as well (see the bottom row). The upper left and right corners appear to be in their best focus closer to the $f = 1$ extreme focus position.

It is clear from all of this that the PSF behavior is

complicated, both spatially and as a function of focus. There is no obvious way to reduce this from a 3-parameter family (x,y,f) to anything simpler. Even so, the behavior with focus and position do appear to be adequately characterized by our empirical modeling.

We have saved our focus-diverse PSF model in a simple four-dimensional fits image that is $101 \times 101 \times 56 \times 11$, where the first two dimensions correspond to the PSF

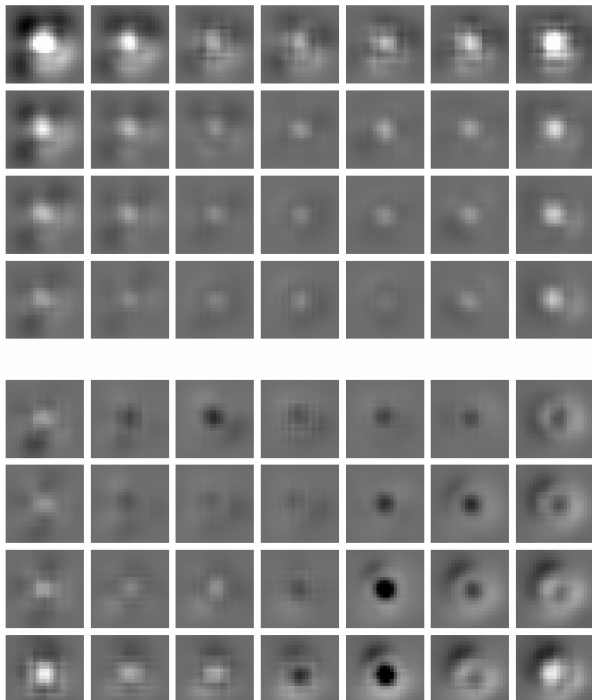


Figure 10. The array of PSFs for the middle focus position ($f=6$), shown with respect to the average across the detector for this focus level. Black corresponds to more flux.

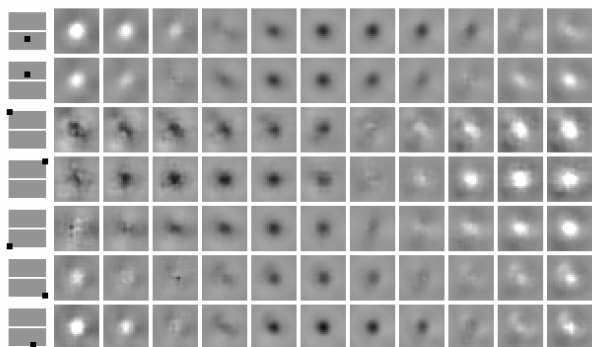


Figure 11. Each row shows the PSF at a different location on the detector, as indicated in the schematic at the left. The panels from left to right then show the central region of the PSF as a function of focus level, with focus level 1 in the leftmost column after the schematic and focus level 11 in the rightmost column. The PSFs are shown relative to the average over all focus levels at that location. Black corresponds to more flux.

model itself. The third dimension (56) corresponds to the 7×8 array of fiducial models, and the fourth dimension (11) corresponds to the focus level. This allows us to construct a PSF for any star at any location of an image with any given focus level.

5 FINDING THE PSF FOR EACH OBSERVATION

Now that we have a focus-diverse PSF model, we can fit it to the stars in a given exposure in order to empirically determine the best focus for that exposure and consequently the best PSF for that exposure. The fact that we have a full spatially variable model for each focus level means that we can use stars from all over the detector to help us determine the focus.

5.1 Using many stars to solve for the focus

To determine the focus for each exposure, we identified a set of about 1000 bright isolated stars in the image. We then fit each star with the model PSF that is appropriate for its location on the detector at a range of focus levels between 1 and 11, stepping by 0.2 focus level (we used linear interpolation to get the PSF between focus levels).

For each fitted star at a given focus level, we determined the optimal (x,y) position and flux and then got an estimate of the quality of fit, which is simply the absolute value of the residuals between observed pixels and PSF model, scaled by the flux of the star. Well-fitted stars tend to have residuals of less than 3%. We determined an average quality of fit for the stars for each focus level and identified the best focus as the one that produced the smallest average residual for all the stars in the image.

We thus determined an empirical focus level for each exposure with a precision of about a fifth of a focus level. Figure 12 shows the focus level determined for the time-sorted exposures within each epoch in the twelve labeled panels. We connect with a solid line those exposures taken within 500 seconds of each other (indicating that they were taken one after another). We reiterate that the focus level for each exposure was determined entirely independently, thus the trends we see reflect real and regular PSF variations.

Some of the epochs exhibit extremely regular variations that repeat every orbit. Others show less regularity. Clearly the focus variations depend both on the telescope's insolation history and how the Sun heats it during its on-source pointing. It is beyond the scope of this study to try to understand these variations, rather our aim is simply to measure the focus and arrive at the best possible PSF. Nevertheless, it is clear that this represents a powerful way to examine focus changes due to short-term breathing or other, possibly longer-term, phenomena such as focus drift.

5.2 How well do individual stars predict focus?

Given the success of the fitting-focus by exposure above, it is worth asking how many stars are needed to pin-down the focus. To examine this, we identified seven images that had focus levels of 1, 3, 5, 6, 7, 9, and 11. For each exposure, we selected 500 or so stars from across the detector that had S/N of 300 or higher. For each individual star, we determined an optimal focus level based on the focus parameter that provided the best quality of fit to the star's central 5×5 pixels.

In Figure 13, we show the fitted focus for each star as a function of instrumental magnitude for the seven chosen exposures in seven different panels. It is clear that most stars

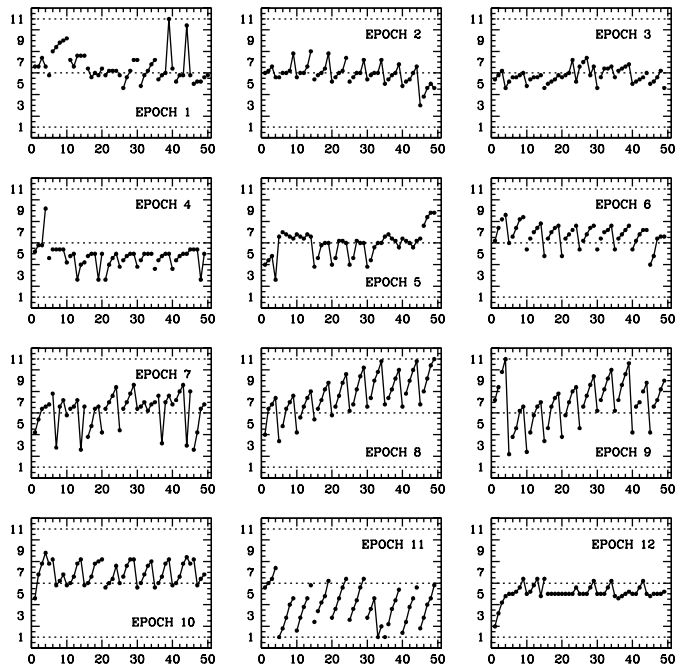


Figure 12. In each of the twelve panels, we show the extracted focus determination for the ~ 50 exposures taken during the corresponding epoch. Exposures are connected with a solid line if they are taken within 500 s of each other.

in the image are excellent predictors of the focus: typically each star can predict the focus to within half a focus level.

To show this even more visually, in Fig.14 we show explicitly the scaled residuals for six stars, probing three different pixel phases at each of two different focus levels. Whereas in A15 we had to restrict our analysis to stars that were centered on pixels in one corner of the detector, here it is clear that with a comprehensive model, the variation with focus can be sensed and calibrated for *all* stars at *all* locations on the detector.

We clearly do not need thousands of stars to pin-down the focus level. Furthermore, it is not clear from Figure 13 how a star’s signal-to-noise will affect our ability to determine focus from it.

To explore this, we took the image in the fifth panel (ic0532ecq), found to have focus level ~ 7 , and determined the focus level for individual isolated stars with S/N from 400 ($m=-13$) to S/N 30 ($m=-7.5$). The red errorbars in Figure 15 show the median and $\pm 1\text{-}\sigma$ range of the distribution within each magnitude bin. It is clear that a handful of stars of moderate flux can pin down the focus to well within a focus level. This is good news, since even sparse fields (such as the UDF) have about 10 stars, several with reasonable S/N. Clearly with focus-diverse PSF models for many more filters it will be possible to characterize the focus level for a large fraction of *HST* images.

5.3 Breathing and Platescale

The *HST* platescale is not constant. As *HST* orbits the Earth and the Earth orbits the Sun, its space velocity is continuously changing. Relativistic velocity aberration (VA)

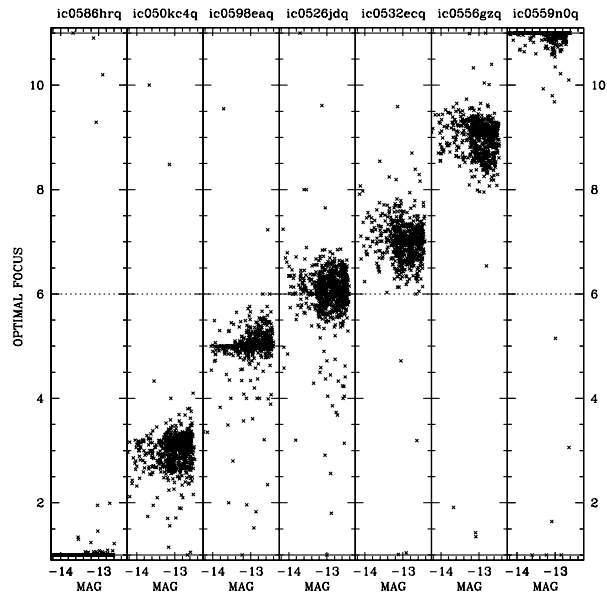


Figure 13. In each panel, we show the focus level as determined independently by several hundred extremely bright but unsaturated isolated stars. The seven panels showcase the results from seven images that span the observed focus range.

can lead to changes in the platescale of up to one part in 10^4 (Cox & Gilliland 2003). The `VAFAC` keyword in the image headers provides a calculation of the VA based on Hubble’s velocity and pointing vectors averaged over the exposure time.

In addition to velocity aberration, breathing can also affect an observation’s platescale, and the 589 exposures of our field give us a unique opportunity to examine the effect of breathing on platescale. For each exposure, we can determine an average platescale by relating the distortion-corrected positions for stars in that frame (x, y) to the positions of stars in the master frame (X, Y). The platescale is simply $\sqrt{AD - BC}$ of that global linear transformation defined by

$$\begin{cases} X = Ax + By + X_0 \\ Y = Cx + Dy + Y_0. \end{cases} \quad (1)$$

The left panel of Figure 16 plots the observed platescale (relative to the average) as a function of the `VAFAC` keyword in the header of each image. Clearly, much of the platescale variation can be explained by VA. The middle plot shows the residual between the observed and VA-predicted platescale. Finally, the right-most plot shows this residual as a function of our determined focus level. It is clear that the same “breathing” that causes changes in focus also causes changes in the amplitude of the platescale up to 0.04-pixels.

6 MAKING USE OF THESE PSFS

Now that we have identified the best-focus PSF for each exposure, it is worth considering how well that PSF actually fits the stars. To do this, we investigated four different PSFs: (1) the “library” PSF we constructed for F467M that

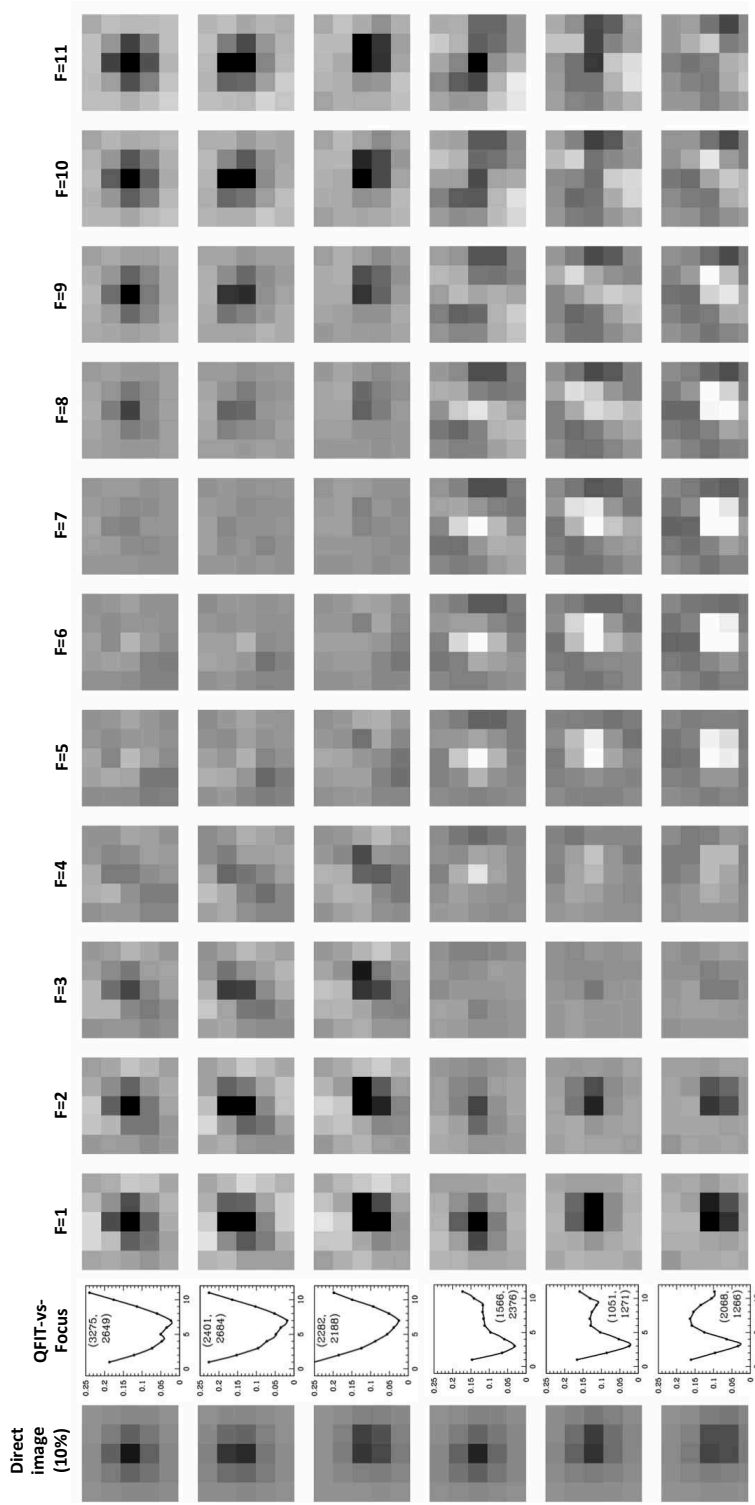


Figure 14. The scaled fitting residuals for six stars, probing three different pixel phases and two images at different focus levels. The left panel shows the 5×5 -pixel cutout of the `_flc` image centered on the star. These were the pixels that the focus-diverse PSF was fitted to. The next panel shows the quality-of-fit metric as a function of assumed focus level. Finally, the eleven rasters show the scaled residuals for the eleven fiducial focus levels. For each fit, we minimized the residuals by allowing the center of the star and its flux to vary freely. Dark corresponds to more flux in the image than in the model. The direct star image on the left is shown scaled down by a factor of 10 relative to the residuals. The top three rows of panels were taken from exposure `ic0532ecq` and the bottom three from `ic050kc4q`.

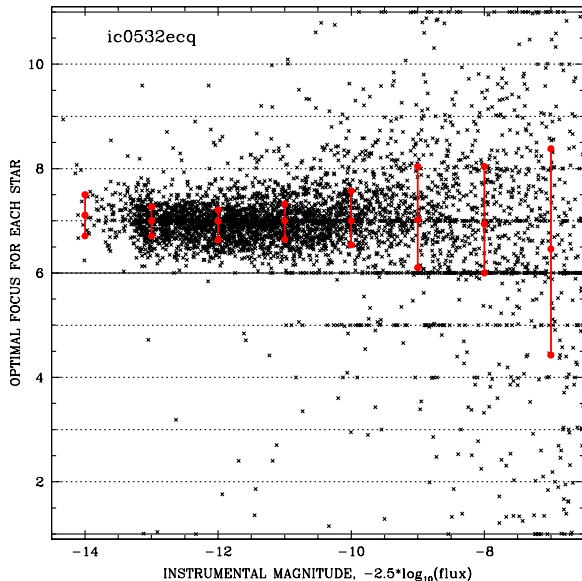


Figure 15. The focus level as determined by isolated stars at a range of brightness in image ic0532ecq (found to have focus level 7). Clearly the bright stars are better predictors of focus, but even a few faint stars can determine the focus quite accurately.

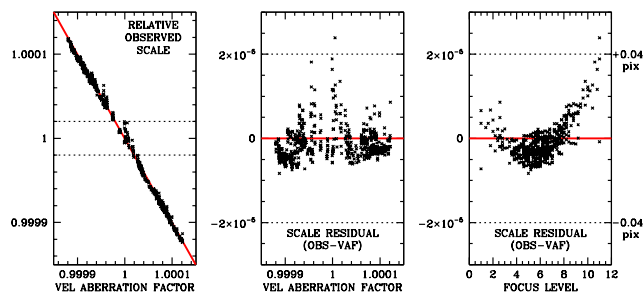


Figure 16. (Left) Observed relative platescale plotted against the velocity-aberration factor keyword (VAFACOR) calculated on the base of the (predicted) telemetry, and provided in the header. (Middle) Difference between observed and predicted scale. (Right) Difference plotted against the determined focus-level for each exposure. The dotted lines correspond to ± 0.04 pixel change at the edge of the detector.

was designed to represent average focus, (2) the fitted-focus PSF, (3) the 4×4 -perturbed library PSF, and finally (4) the 4×4 -perturbed fitted-focus PSF. In these images taken at the center of M4, we have enough stars to construct a perturbation for each image’s PSF. In many fields, we will barely have enough stars to pin down the focus, meaning that there is no way to construct a perturbation PSF for them.

There are several metrics available to evaluate PSFs, such as quality of fit and photometry and astrometry. When we fit a star with the PSF, we determine sky from a remote annulus and fit the star’s inner 5×5 pixels with the PSF by finding the (x, y) location and flux that minimize the residuals in a least-squares sense, taking into consideration the

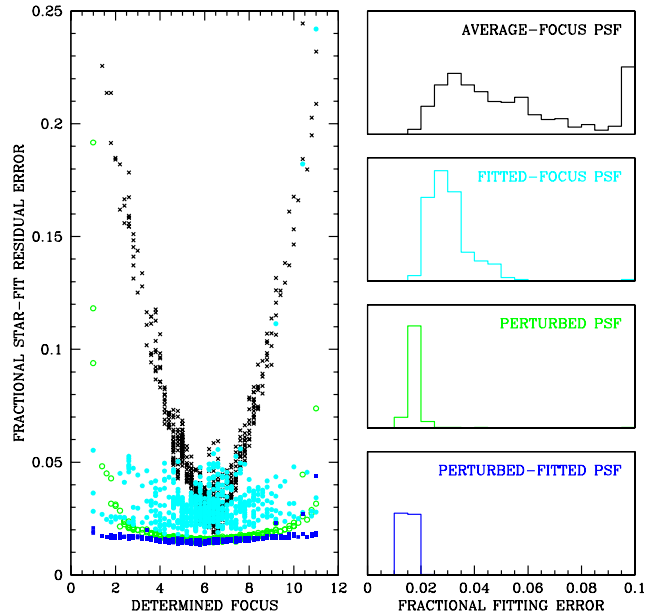


Figure 17. (Left) The average fractional star-fit residual for each exposure, plotted as a function of extracted focus for four different PSF treatments, as labeled on right. (Right) Histograms of star-fit residuals for the four treatments.

Poisson error in each pixel. Since it is not a time-consuming process, we simply do a grid search for (x, y) and at each trial position, determine the flux by simple aperture photometry (knowing from the PSF what fraction of the star’s light should fall within the aperture based on its trial position). Once we have a best-fit position, we determine the total absolute residual between the observations and model and divide by the total flux to get a scaled residual.

Figure 17 shows the average fitting residual for the bright stars within 1.5 magnitudes of saturation for each of the 589 exposures as a function of fitted focus for that exposure. The black points show the fitting error for the unperturbed temporally constant “library” PSF. The cyan points show the residuals for the fitted-focus PSF. The green points show the perturbed library PSF, and the blue points show the residuals for the perturbed focus-fitted PSF. It is clear that the blue points have fitting residuals smaller than 2% for all focus levels. The perturbed library PSF is almost as good, but it loses quality when the focus is considerably off nominal. The focus-fit PSF has residuals of about 3% everywhere, and the library PSF has about 4% errors when the focus is good, but has a trail to well over 20% errors when the focus is off. The histograms on the right show the same data summed over all focus levels.

One of the most obvious effects of breathing is that the fraction of light in the core of the PSF changes. When fluxes for stars are determined by fitting a “library” PSF to the core, breathing results in photometric zero-point shifts from exposure to exposure, typically ± 0.03 magnitude, but sometimes more. Figure 18 shows the measured photometric zero-point shift between each exposure and the average for the 589 F467M exposures for the four different PSF approaches adopted. The constant “library” PSF has typical zero-point

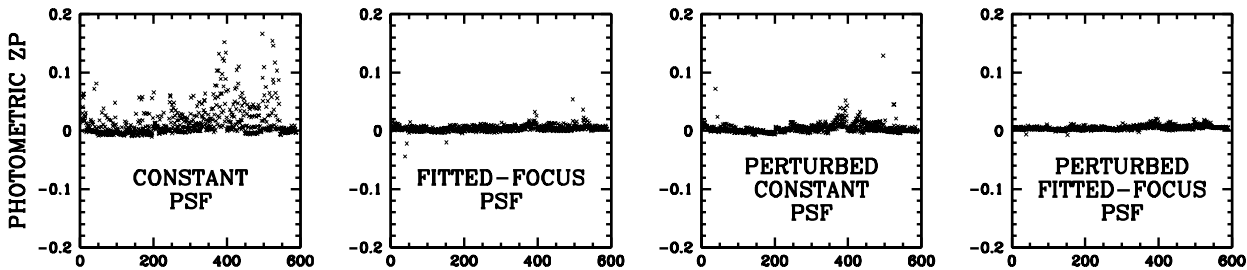


Figure 18. The empirical photometric zero-point shifts for the four different PSF treatments plotted against exposure number.

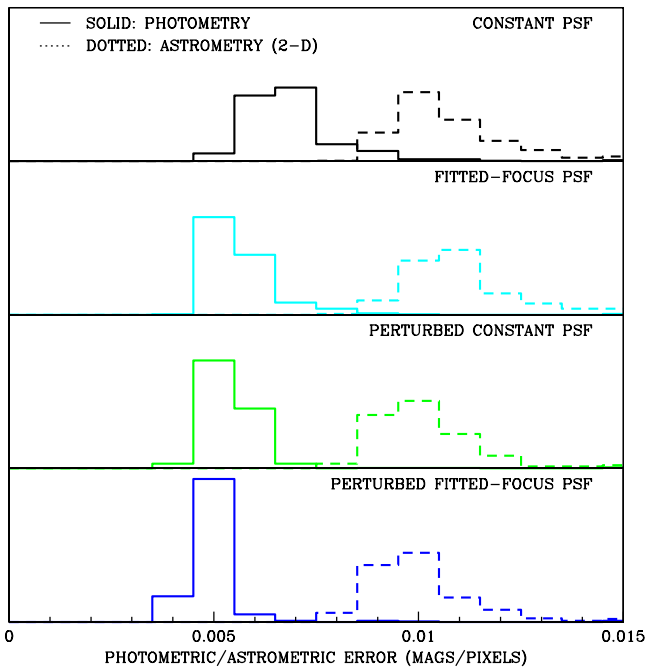


Figure 19. Distribution of RMS photometric residuals (solid) and 2-D astrometric residuals (dotted) for the four different PSF treatments.

shifts of about ± 0.02 magnitude, but they can be greater than 0.15 mag. The other PSF approaches have shifts generally less than 0.01 magnitude, though it is worth noting that the fitted-focus PSF does better than the perturbed library PSF. Not surprisingly, the perturbed fitted-focus PSF does best.

The photometric and astrometric residuals are the most basic test of a PSF. Figure 19 shows histograms of the photometric (solid) and 2-D astrometric (dotted) RMS residuals for the brightest unsaturated stars. In computing these residuals, we have each exposure to have an arbitrary photometric zero-point and have allowed a general 6-parameter linear transformation to match the distortion-corrected frame of each image to the reference frame.

It is not surprising that if we allow for an arbitrary zero-point, the photometry does not improve much with the improved PSF. (It improves by 15% from 0.0065 magnitude to 0.005 magnitude RMS). This may sound surprising, since

Figure 9 showed a 20% variation in the core intensity with focus changes. Clearly most of the variation with focus involves shifting within the 5×5 -pixel aperture we used (say, from the core to the first diffraction ring). Some variation, though, does shift light from within the 5×5 -pixel aperture to outside the aperture, and this appears to happen similarly for stars across the detector, such that a single zero-point shift for each filter addresses much of it.

We see a similar effect with the astrometry. If we allow for an arbitrary scale change (included in the linear transformation), then the astrometry is not much different for the four different PSFs: we achieve about 0.007-pixel precision per coordinate. This indicates that the shape of the PSF core does not change much with focus.

The slight improvement of the astrometry is actually good news. The original “library” (average focus) PSF was constructed carefully from a dithered set of data so that the undersampled PSF could be properly derived free of pixel-phase bias (see Section 2.2 of Anderson & King 2000 for a discussion). This PSF was used for the extraction positions in our PSF reconstructions here with no additional positional constraints, so it is reassuring that the PSFs constructed are even slightly better in an astrometric sense. It is also the case that the distortion solution was derived based on positions measured with the “library” PSF, and it is clear that the positions measured with the focus-diverse PSFs (and various perturbed PSFs) are no less accurate in a systematic sense.

7 F775W PSF

Program GO-12911 also included a short 20s F775W exposure in nine out of ten of the orbits available within each of the twelve epochs, for a total of 108 short F775W exposures. This is enough for a preliminary examination of the variation in that PSF. As above with F467M, we used a “library” F775W PSF to fit the stars in each exposure and developed a 4×4 array of perturbation PSFs to match the library PSF to the image PSF.

Figure 20 is the F775W analog for F467M’s Figure 6. The lower-right panel shows the “phylogram” plot for the F775W images, with the regions from F467M marked in blue. As before, the distance between PSFs corresponds to the average amount of flux that would have to be redistributed to get from one to the other. Whereas we would have to arrange up to 30% of the flux to get from one F467M

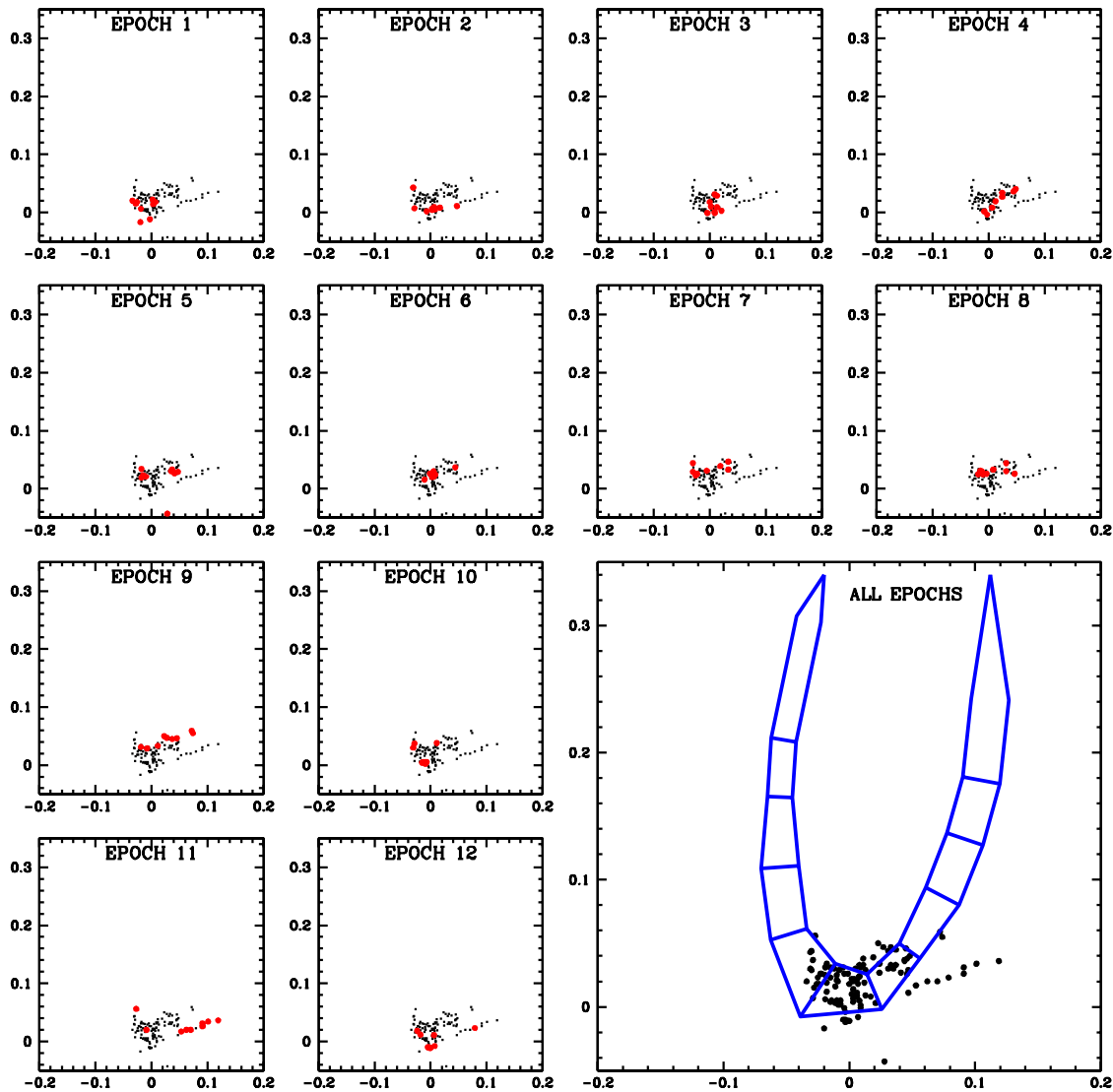


Figure 20. The “phylogram” plot for F775W. It is clear that the PSF does not vary nearly as much for this redder filter.

PSF to another focus level, we would have to rearrange at most 10% of the F775W PSF.

An additional consideration that arises when modeling the PSFs for a wide-band filter is the fact that blue star and red stars can have somewhat different effective wavelengths due to their different spectral-energy distributions (SEDs). If we are able to come up with a focus-diverse set of PSFs for wide-band filters, it might be possible to introduce an additional parameter to deal with the color of the stars, but that is beyond the scope of this effort.

8 CONCLUSIONS

We have made use of the uniform dataset of GO-12911 to explore and model the variation of the F467M PSF in great detail. We have shown that, by and large, the PSF varies in predictable ways along a single-parameter curve, where the single parameter is related to the telescope focus.

We have grouped together images that were taken at similar focus levels and have constructed for each of eleven focus levels a full spatially variable representation of the PSF (i.e., with 7×4 across each of the two 4096×2048 chips). We have examined this PSF and find that—as expected—at nominal focus (where most of the exposures are taken), the PSF is sharpest at the centers of the chips. For the corners of

the chips, the PSF is actually sharpest at off-nominal focus positions.

Although in a previous work (Anderson et al 2015), we made use of the fact that the upper-left corner is particularly sensitive to focus changes in order to study PSF changes with focus, we find here that the PSF across the entire detector is actually quite sensitive to focus. If we fit a typical, bright ($S/N > 50$) star with PSFs at a range of trial focus levels, we find that we can identify the image focus to better than 1 focus level (out of eleven). With only a handful of stars, it should be possible to pin-down the focus level of *any* exposure. This will make it possible to construct a tailor-made PSF for every deep exposure, since a typical deep field has at least five stars with reasonable signal.

The PSF model we constructed here is for F467M, admittedly an uncommon filter. However the procedure we developed can be used for the entire archive: it does not depend on the fact that we are observing the same field in all the exposures. Therefore it should be possible to construct a focus-diverse PSF model for all of the common WFC3/UVIS filters. The WFC3/UVIS instrument team is currently pursuing this, as such a detailed understanding of focus changes will allow the engineers to make better determinations of when to re-adjust focus. Having access to a robust empirical focus measurement will also help engineers at the *Space Telescope Institute* to develop a more accurate model of how telemetry and environmental data may be better able to predict focus variations.

Overall, we find that the focus-diverse PSFs represent a significant improvement in the quality of fit for sources and in the absolute photometric zeropoint for exposures, the improvement is particularly significant when the telescope is out of focus. The new PSFs also represent a modest—although measurable—improvement in the photometric and astrometric precision. As such, they will clearly make the biggest difference for point-source/galaxy discrimination, detailed PSF-fitting to resolved or slightly resolved objects, and for absolute-catalog work.

The particular M 4 project at hand (GO-12911), which has enabled this detailed PSF study, will benefit of this improved PSFs, not only directly through the marginally improved astrometric and photometric precision, but also because of the significant improvement in the PSFs shape, which will help to better disentangle blends from isolated stars. Therefore, we will use the perturbed focus-diverse in our high-precision astrometric wobble analysis, which is the next step for the project.

ACKNOWLEDGMENTS

JA acknowledges support from STScI grant GO-12911. LRB acknowledges PRIN-INAF 2012 funding under the project entitled: ‘*The M 4 Core Project with Hubble Space Telescope*’. We would like to thank Elena Sabbi, Linda Dressel, Kailash Sahu, and Matthew Bourque for many useful discussions in the course of this work.

REFERENCES

Anderson, J. & King, I. R. 2000, PASP, 112, 1360, (AK00)

Anderson, J. & King, I. R. 2006, ACS/ISR 06-01, STScI, Baltimore

Anderson, J. & King, I. R. 2004, ACS/ISR 04-15, STScI, Baltimore

Anderson, J. 2016, WFC3/ISR 2016-12, STScI, Baltimore

Anderson, J. et al. 2015, WFC3/ISR 2015-08, STScI, Baltimore, (A15)

Anderson, J. & Bedin L. R. 2010, PASP, 122, 1035

Bedin, L. R. et al. 2013, AN, 334, 1062, (Paper I)

Cox, C., Gilliland, R. L., 2003, in Arribas S., Koekemoer A., Whitmore B., eds, *The 2002 HST Calibration Workshop: Hubble after the Installation of the ACS and the NICMOS Cooling System*. STScI, Baltimore, p. 58

Cox, C. & Niemi, S. 2011 ISR/TEL-2011-01, STScI, Baltimore

Dressel, L. 2014, ISR/WFC3-2014-14, STScI, Baltimore

Krist, J., 2006, ISR/ACS-2003-06,

Lauer, T., 1999, PASP, 111, 1434

Sabbi, E. & Bellini, A. 2013, Instrument Science Report WFC3, 2013-011, STScI, Baltimore, (SB13)